Physics of Plasmas

Effects of resonant magnetic perturbations on neutral beam heating in a tokamak

Cite as: Phys. Plasmas **28**, 122502 (2021); https://doi.org/10.1063/5.0069792
Submitted: 02 September 2021 • Accepted: 25 November 2021 • Published Online: 16 December 2021

Youjun Hu, Yingfeng Xu, Baolong Hao, et al.

Physics of Plasmas ARTICLE scitation.org/journal/php

Effects of resonant magnetic perturbations on neutral beam heating in a tokamak

Cite as: Phys. Plasmas **28**, 122502 (2021); doi: 10.1063/5.0069792
Submitted: 2 September 2021 · Accepted: 25 November 2021 ·
Published Online: 16 December 2021

Youjun Hu,[1] Yingfeng Xu,[2,a)] Baolong Hao,[3] Guoqiang Li,[1] Kaiyang He,[1] Youwen Sun,[1] Li Li,[2] Jinfang Wang,[1] Juan Huang,[1] Lei Ye,[1] Xiaotao Xiao,[1] Feng Wang,[4] Chengkang Pan,[1] and Yongjian Xu[1]

AFFILIATIONS

[1]Institute of Plasma Physics, Chinese Academy of Sciences, Hefei 230031, China
[2]College of Science, Donghua University, Shanghai 201620, China
[3]Advanced Energy Research Center, Shenzhen University, Shenzhen 518060, China
[4]School of Physics, Dalian University of Technology, Dalian 116024, China

[a)]Author to whom correspondence should be addressed: xuyingfeng@dhu.edu.cn

ABSTRACT

The effects of resonant magnetic perturbations (RMPs) on tangential neutral beam heating in the EAST tokamak are studied numerically. RMPs with linear resistive magnetohydrodynamics response are used in the modeling. A variety of representing configurations of RMP coil currents are examined, and their effects on the neutral beam injection (NBI) heating efficiency are compared, in order to find a parameter window where deleterious effects of RMPs on NBI heating efficiency are minimized. It is found that the internal redistribution of fast ions by RMPs induces local accumulation of fast ions, resulting in higher local fast ion pressure than the case without RMPs. It is also found that the toroidal phasing of the RMP with respect to the fast ion source has slight effects on the steady-state radial profile of fast ions. The dependence of fast ion loss fraction on the RMP up-down phase difference shows a similar behavior as the dependence of the radial width of chaotic magnetic field on the phase difference. A statistical method of identifying resonances between RMPs and lost fast ions is proposed, and the results indicate that some resonances between RMPs and lost passing particles may be of non-integer fractional order, rather than the usual integer order.

I. INTRODUCTION

Neutral beam injection (NBI) is widely adopted in tokamaks for heating plasma and driving flow.[1–5] Modeling the neutral beam heating, which involves neutral particle ionization and fast ion collisional transport, is a mature field where simulation results usually agree reasonably with experiments.[6] One of the uncertainties in the modeling is how electromagnetic perturbations, if present, affect the heating and fast ion transport process. These electromagnetic perturbations can be various intrinsic modes, such as Alfvén eigenmodes, and can also be externally imposed perturbations, such as resonant magnetic perturbations (RMPs).

This work numerically studies the influence of RMPs on the deuterium neutral beam heating in the EAST tokamak.[7,8] EAST is equipped with RMP coils, which are designed for the control of edge localized modes (ELMs).[9,10] This coils turn out to also have effects on the transport of neutral beam fast ions.[11–15] The effects of RMPs on fast ion transport and loss have been extensively investigated on AUG,[16–18] KSTAR,[19] DIII-D,[20,21] and MAST[22] tokamaks.

In this work, we consider RMPs of $n=1$ with linear resistive magnetohydrodynamics (MHD) plasma response, where n is the toroidal mode number of the RMP coil current. The configurations with $n=0,2,3,4$ were also examined (not shown in this paper). The results indicate that $n=0$ RMP has negligible effects on the confinement of fast ions, as is expected, and the deleterious effects of configurations with $n=2$, 3, 4 on the confinement of fast ions are generally smaller than that of the $n=1$ RMP. Therefore, we will focus on the $n=1$ configuration in this paper.

We consider one of the four neutral beams on EAST that is injected in the co-current direction, with the tangent radius being 1.26 m and the full (kinetic) energy being 51 keV. The number ratio between neutrals of the full energy, half energy, and 1/3 energy is chosen to be 80 : 14 : 6. NBI power after neutralizing is assumed to be 1 MW. Further details on the neutral beam modeling are provided in Appendixes A and B. In this paper, fast ions are defined as those ions that are born from the neutral beam ionization and have not yet been slowed down to the energy $2T_{i0}$, where T_{i0} is the temperature of background thermal ions at the magnetic axis.

We found that the internal redistribution of fast ions by RMPs can induce local accumulation of fast ions, resulting in larger local fast ion pressure than the case without RMPs. It is also found that the toroidal phasing of the RMP with respect to the fast ion source has slight effects on the steady-state radial profile of fast ions. The dependence of fast ion loss fraction on the RMP up-down phase difference $\Delta\Phi$ is found to show a similar behavior as the dependence of the radial width of chaotic magnetic field on $\Delta\Phi$.

A simple statistical method for identifying resonances between RMPs and lost fast ions is proposed, in which resonances are identified by examining peaks in the graph of p vs Δf, where $p = n\omega_\phi/\omega_\theta$ is called the resonance order with ω_ϕ and ω_θ being the toroidal angular frequency and poloidal angular frequency of lost fast ions, respectively, and Δf is the difference of the lost fast ion distribution function between the case with RMP and that without RMP. By taking the difference, we exclude all the fast ions that are lost due to the first-orbit prompt loss and pure collision loss. The results indicate that some resonances may be of non-integer fractional order, rather than the usual integer order.

In the process of studying the effects of RMP on NBI heating, we developed a new Monte Carlo code, which models continuous neutral beam injection, ionization, and the resulting fast ions transport under the influence of RMPs. This code (referred to as `TGCO`) is similar to the established NBI modeling code `NUBEAM`[6] and many other test particle orbit-following codes, such as `OFMC`,[23] `ASCOT`,[24] `ORBIT`,[25] `SPIRAL`,[26] `VENUS-LEVIS`,[27] `GYCAVA`,[12] and `SOFT`.[15] `TGCO` has been used as a NBI module in Refs. 11, 14, and 28. The guiding-center drift model, edge loss model, and fast ion collision model adopted in this work are well known, and the details of these models are provided in the Appendix. The finite Larmor radius (FLR) effect is taken into account when pushing particle guiding center drift, depositing markers to compute density and pressure, and checking whether particles are lost to the boundary. The simulation includes the X-points of equilibrium magnetic field and uses the first wall as the particle loss boundary. For simplicity, we assume a pure deuterium plasma with no impurities.

The remainder of this paper is organized as follows. Section II describes the equilibrium configuration, bulk plasma profiles, and neutral beam ionization profiles. Section III introduces the RMP coils on EAST and the resulting 3D magnetic perturbations with/without plasma response. Section IV discusses the effects of RMPs on the steady state radial profiles of neutral beam heating and fast ion pressure. Section V examines the dependence of volume integrated heating power, fast ion stored energy, and fast ion loss fraction on the up-down phase difference of RMP coil currents, where radial width of chaotic magnetic region is computed and is found to be closely related to the fast ion loss fraction. Section VI use a statistical method to identify the resonance between RMPs and fast ions. A brief summary and some discussions are given in Sec. VII.

II. EQUILIBRIUM AND FAST ION SOURCE

EAST is a superconducting tokamak with a major radius $R_0 = 1.85$ m, minor radius $a \approx 0.45$ m, typical on-axis magnetic field strength $B_{\text{axis}} \approx 2.2T$, and plasma current $I_p \approx 0.5$ MA.[7,8] The magnetic configuration and plasma profiles used in this work (Fig. 1) were reconstructed by EFIT code from EAST tokamak discharge #52340@3.4s with constrains from experiment diagnostics.

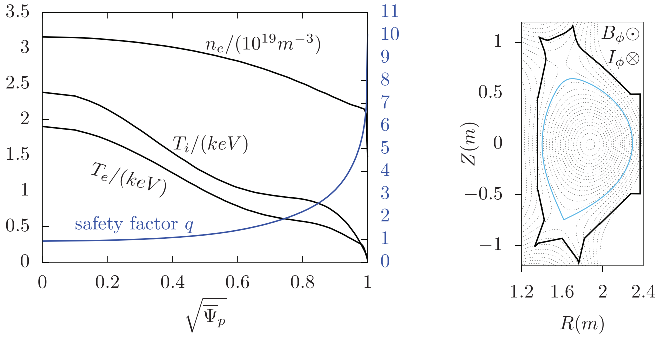

FIG. 1. Left panel: profiles of electron number density n_e, electron temperature T_e, ion temperature T_i, and safety factor q of EAST discharge #52340@3.4s. The radial coordinate $\rho = \sqrt{\bar{\Psi}_p}$ is the square root of the normalized poloidal magnetic flux, with $\bar{\Psi}_p = (\Psi - \Psi_0)/(\Psi_b - \Psi_0)$, where $\Psi \equiv A_\phi R$ is the poloidal flux function, Ψ_0 and Ψ_b are the values of Ψ at the magnetic axis and last closed-flux surface, respectively. Right panel: magnetic configuration. This is a low single null configuration with $B_{\text{axis}} = 2.2T$, $I_p = 404$kA, $q_{\text{axis}} = 0.95$, and $q_{95} = 5.05$.

The neutral beam ionization is modeled by the Monte Carlo method, and the details are provided in Appendix B. Figure 2 plots the two-dimensional distribution of ionized particles in the poloidal plane (averaged over the toroidal direction) and in the toroidal plane (averaged over the vertical direction). The results indicate most of the fast ions are born on the low-field-side.

Figure 3 plots the distribution of ionized particles in (Λ, P_ϕ) plane and (λ, R) plane, where $\Lambda = \mu B_{\text{axis}}/\varepsilon$, $\lambda = v_\parallel/v$, ε is ion kinetic energy, and P_ϕ is the canonical toroidal angular momentum. The trapped/passing boundary in (Λ, P_ϕ) plane is plotted, which indicates that most ions born in this case are in the passing region, with a small number of ions being near the trapped/passing boundary.

III. THREE-DIMENSIONAL MAGNETIC PERTURBATIONS

EAST has 16 RMP coils consisting of two arrays of eight coils with up-down symmetry located on the low field side and uniformly distributed along the toroidal direction. Figure 4 shows the setup of the RMP coils on EAST tokamak.[9]

The vacuum magnetic perturbations produced by the RMP coils are numerically calculated by using the Biot–Savart law. The magnetic

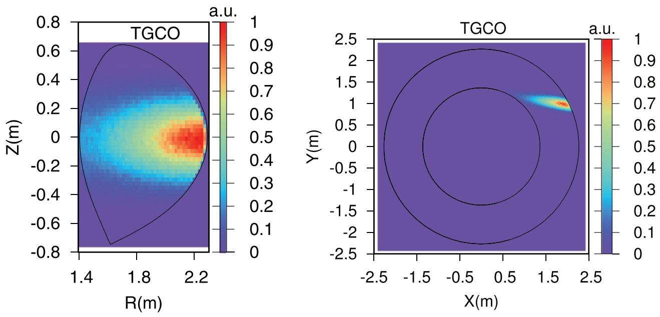

FIG. 2. Neutral beam ionization profiles in the poloidal plane (left) and toroidal plane (right) computed by TGCO. This is for the neutral beam injection with $R_{\tan} = 1.26$ m in EAST discharge #52340@3.4s. The loss fraction of neutral particles to the inner first wall (shine-through loss) is 14% in this case.

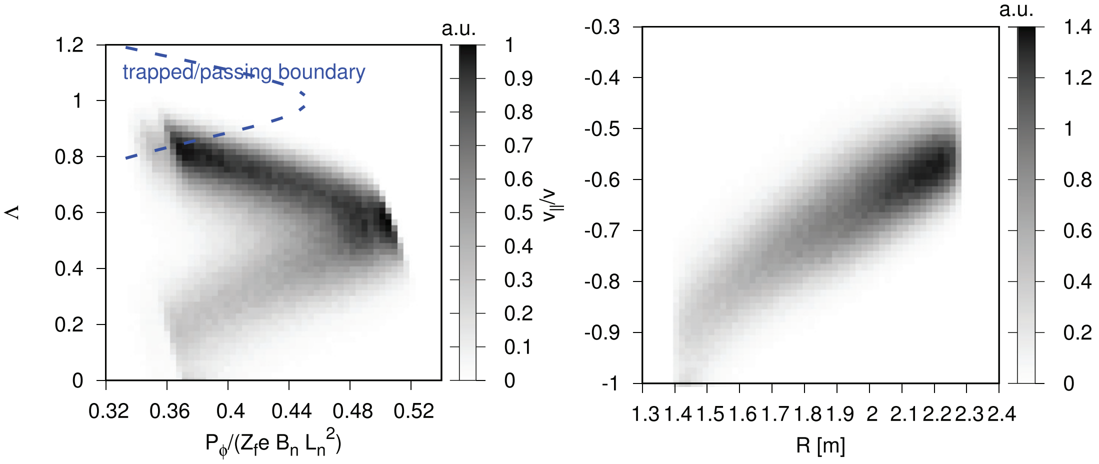

FIG. 3. Distribution of ionized particles in (Λ, P_ϕ) plane (left) and (λ, R) plane (right), where $\Lambda = \mu B_{\rm axis}/\varepsilon$, $\lambda = v_\parallel/v$, $P_\phi = m_f g v_\parallel/B_0 + Z_f e\Psi$ is the canonical toroidal angular momentum, μ is the magnetic moment, $v_\parallel$ is the parallel (to the magnetic field) velocity, B_0 is the equilibrium magnetic field, m_f and $Z_f e$ are the mass and charge of fast ions, respectively, $g = B_\phi R$, $B_n = 1T$, $L_n = 1m$. The trapped/passing boundary in (Λ, P_ϕ) plane is indicated (the region to the left side of the curve is the trapped region).

perturbations including the effect of plasma response are computed, using the linear resistive MHD model, by MARS-F code[29,30] as a boundary value problem, taking into account of a given toroidal flow. The RMP coil current, located in the vacuum region outside the plasma, is directly modeled in the code as a source term.[30]

In this work, we use the $n=1$ RMP with a current amplitude of 10 kAt unless otherwise specified. To perceive the magnitude of the resulting magnetic perturbation (without plasma response) relative to the equilibrium field, Figs. 5(a) and 5(d) show the two-dimensional distribution of $\delta B/B_0$ on the $\rho = 0.96$ magnetic surface. Figures 5(b) and 5(e) show the poloidal dependence of $\delta B/B_0$ at a series of toroidal locations at $\rho = 0.96$ and Figs. 5(c) and 5(f) show the toroidal dependence of $\delta B/B_0$ at a series of poloidal locations at $\rho = 0.96$. The results indicate that the maximal value of δB at $\rho = 0.96$ is about 0.3% of the equilibrium field B_0. The corresponding minimal value of δB is small (0.03% of B_0), but is not exactly zero.

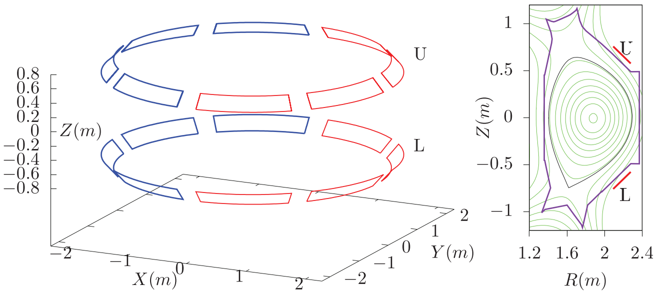

FIG. 4. RMP coils on EAST tokamak in 3D view (left) and poloidal view (right). Each coil has 4 turns with maximum current 2.5 kA per turn. The maximum frequency of alternating current (AC) operation is 1 kHz (usually operating at less than 10 Hz). This paper considers only direct current (DC) operation, i.e., static RMP. In the left panel, red color denotes current circulating in the clockwise direction and blue denotes current circulating in the anti-clockwise direction, viewed from the outside of the torus. The magnitudes of currents are set to be the same. The setup shown here is called $n=1$ and $\Delta\Phi = 0$ configuration, where $\Delta\Phi$ is the up-down phase difference.

The magnetic perturbation component that is perpendicular to the 2D equilibrium magnetic surface (i.e., the radial component) is of most interest to magnetic confinement since it creates magnetic islands at resonant surfaces and thus changes the topology of magnetic field. Define the normalized radial component of the magnetic perturbation by

$$\delta B_N = \frac{\delta \mathbf{B}\cdot\nabla\rho}{\mathbf{B}_0\cdot\nabla\phi}. \tag{1}$$

Fourier expansion of δB_N is written as

$$\delta B_N(\rho,\theta,\phi) = \sum_{n=-\infty}^{\infty} \delta B_N^{(n)}(\rho,\theta)\exp\left[-in\phi\right], \tag{2}$$

$$= \sum_{n=-\infty}^{\infty}\sum_{m=-\infty}^{\infty} \delta B_N^{(mn)}(\rho)\exp\left[i(m\theta - n\phi)\right], \tag{3}$$

where m and n are the poloidal and toroidal mode numbers, respectively, and $\delta B_N^{(n)}$ and $\delta B_N^{(mn)}$ are the Fourier expansion coefficients.

Figure 6 compares the amplitude of $n=1$ harmonic of δB_N in the poloidal plane between the vacuum RMP and the response RMP. The results indicates that the amplitude of perturbation is enhanced by the plasma response at some poloidal locations, which might be related to the kink response.[32] The results also show that there is also some minor perturbation appearing near the top region in the case of response RMP, and there is a twist effect on the distribution of $|\delta B_N^{(1)}|$ by the plasma response.

Figure 7 shows the distribution of magnetic perturbation δB_N over (ϕ, θ) on the $\rho = 0.96$ magnetic surface. Three kinds of perturbations are shown: the full vacuum RMP, the filtered vacuum RMP (keeping only the $n = \pm 1$ Fourier components), and the filtered response RMP. One-dimensional distributions along ϕ at fixed values of poloidal angle θ are also show in Fig. 7 to compare the amplitude

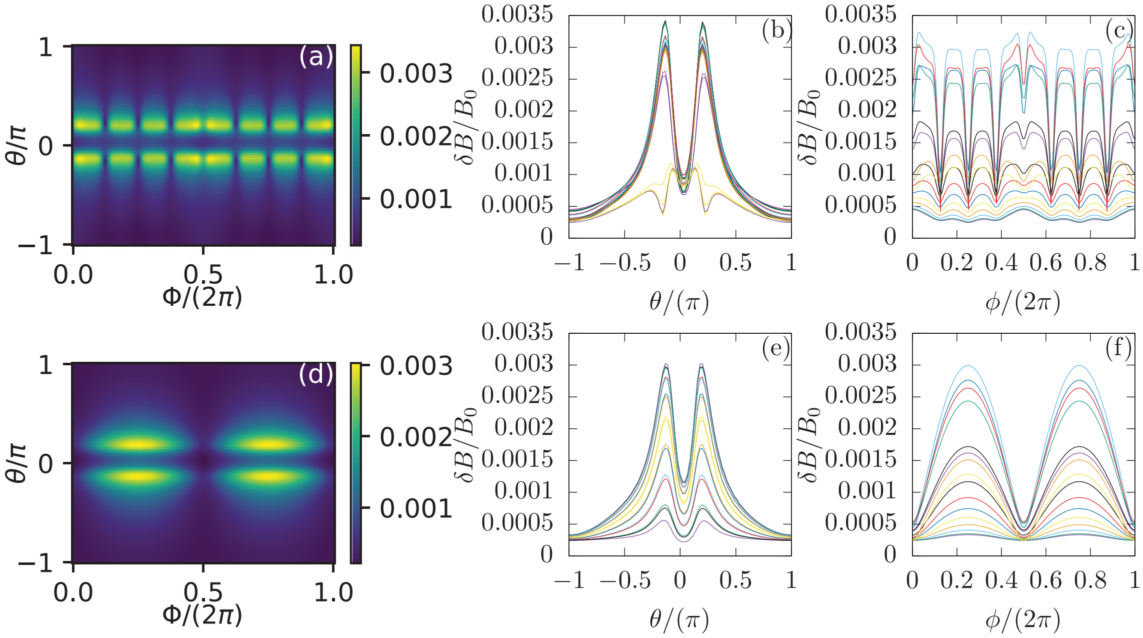

FIG. 5. (a) and (d): Two-dimensional distribution of $\delta B/B_0$ on the $\rho = 0.96$ magnetic surface. (b) and (e) Poloidal dependence of $\delta B/B_0$ at a series of toroidal locations at $\rho = 0.96$. (c) and (f) Toroidal dependence of $\delta B/B_0$ at a series of poloidal locations at $\rho = 0.96$. The upper panels are for the full vacuum field and the lower panels are for filtered vacuum field (keeping only $n = \pm 1$ Fourier harmonics). $\delta B = |\delta \mathbf{B}|$ is the magnetic perturbation magnitude and B_0 is the local value of the equilibrium magnetic field. ϕ is the toroidal angle in the (R, ϕ, Z) cylindrical coordinates. The poloidal angle θ is chosen to be of the PEST type,[31] i.e., magnetic field lines are straight in (θ, ϕ) plane (the positive direction of θ is chosen to be counterclockwise when viewed along $\nabla\phi$ direction; $\theta \in [-\pi, \pi]$ with $\theta = -\pi$ being in the high field side midplane.) The two peaks of $\delta B/B_0$ in the poloidal direction appears near the poloidal locations of the RMP coils. The RMP up-down phasing $\Delta\Phi = 0$ in this case.

and phase along the toroidal direction between the three kinds of magnetic perturbations. The results indicate that the amplitude of perturbation are enhanced by the plasma response at some poloidal locations [Fig. 7(d) and 7(f)] but are slightly reduced at others [Fig. 7(e)]. The results also indicate that the response RMP has a toroidal phase shift relative to the vacuum one, which ranges from minor difference [in Fig. 7(d)] to major difference [anti-phasing in Fig. 7(g)].

To clearly distinguish the resonant components from the nonresonant ones, Fig. 8 gives the heatmap of Fourier components of δB_N in the (m, ρ) plane. Figure 8 compares the poloidal Fourier spectrum of the $n = 1$ harmonic of δB_N between the vacuum RMP and response RMP. The main difference between vacuum and response RMPs is that plasma response reduces the perturbation amplitude at resonant locations (shielding effects) and enhances the amplitude of nonresonant components, as is shown in Fig. 8, where the resonant locations $m = nq$ are indicated.

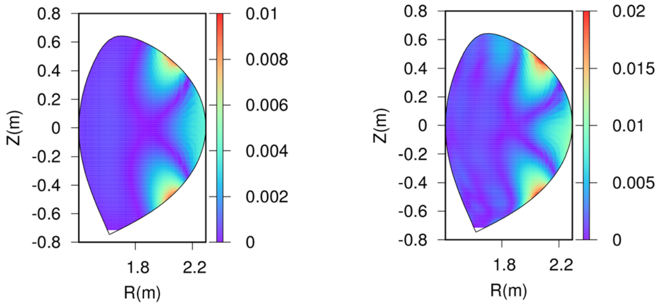

FIG. 6. Amplitude of $n = 1$ harmonic of δB_N, i.e., $|\delta B_N^{(1)}|$, in the poloidal plane. The left panel is for the vacuum RMP and the right panel is for the response RMP.

To more clearly show the effects of plasma response, Fig. 9 compares the radial profiles of amplitude of poloidal harmonics between vacuum RMP and response RMP. The results indicate that the peaks of the harmonics are shifted inward to the core by the plasma response and the peak values near the edge are enhanced. The results also show that plasma response reduces the magnitude of harmonics near their respective resonant locations (e.g., $m = 2$ at $\rho = 0.76$ and $m = 3$ at $\rho = 0.89$).

Using $\delta B_N^{(mn)}$ defined above, the width of magnetic island generated by a magnetic perturbation at a rational surface $q = m/n \equiv q_s$ is given by[33]

$$w_{mn} = 4\sqrt{\left|\frac{\rho\delta B_N^{(mn)}}{nS}\right|_{q=q_s}}, \tag{4}$$

where $S \equiv \rho q'/q$ with $q' = dq/d\rho$ being the magnetic shear. Formula (4) will be used later in this paper to calculate the Chirikov parameter to determine whether adjacent islands overlap. The Chirikov parameter is defined by

$$\sigma = \frac{w_{m_1 n} + w_{m_2 n}}{2|\rho_2 - \rho_1|}, \tag{5}$$

where ρ_1 and ρ_2 are the radial coordinates of two adjacent rational surfaces, and $w_{m_1 n}$ and $w_{m_2 n}$ are the width of magnetic islands at the

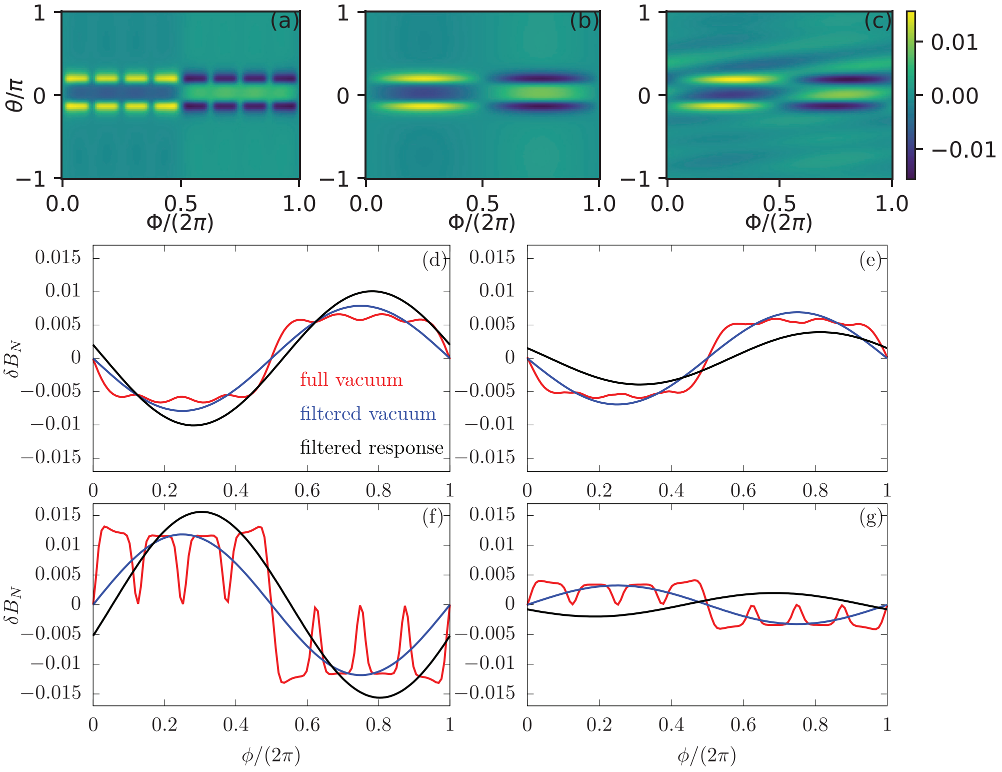

FIG. 7. Distribution of magnetic perturbation δB_N over (ϕ, θ) on the $\rho = 0.96$ magnetic surface. (a)–(c) are for the two-dimensional distributions. (d)–(g) are for the one-dimensional distributions along ϕ at fixed values of poloidal angle θ. Specifically, (d) is for $\theta = 0$, (e) is for $\theta = 0.09\pi$, (f) is for $\theta = 0.18\pi$, and (g) is for $\theta = 0.29\pi$. Three kinds of perturbations are shown: magnetic perturbation produced by the coils (full vacuum), the filtered vacuum field, and the filtered perturbation when the plasma response is considered (filtered response). (a) is for the full vacuum field, (b) is for the filtered vacuum field, and (c) is for the filtered field with plasma response.

two radial locations. Then, the two islands overlap if $\sigma > 1$, which further indicates that magnetic stochasticity appears.

In the remainder of this paper, RMPs refer to the RMPs with plasma response unless otherwise specified.

IV. MODIFICATION OF RADIAL PROFILE OF ION HEATING POWER DENSITY BY RMPS

With continuous beam injection into a time-independent background plasma, a steady state of fast ions can be reached on the

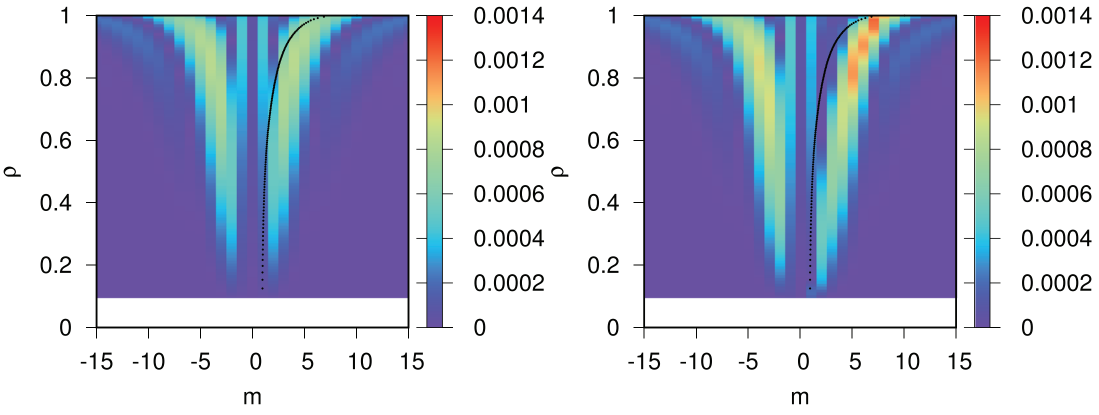

FIG. 8. Amplitude of the poloidal Fourier spectrum of the $n = 1$ harmonic of δB_N for different radial locations, i.e., $|\delta B_N^{(mn)}(\rho)|$ with $n = 1$. The left panel is for the vacuum field and the right panel is for the field with plasma response. RMP coil configuration of $\Delta\Phi = 0$ is used. The black curves are $m = nq$, which indicates the resonant locations.

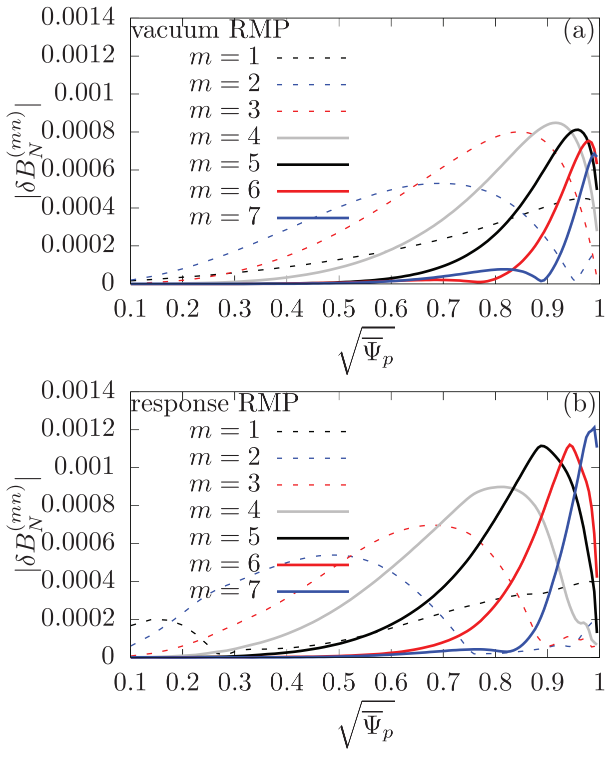

FIG. 9. Radial profile of amplitude of various poloidal Fourier harmonics of $n=1$ RMPs of phasing $\Delta\Phi=0$ for the vacuum case (a) and plasma response case (b). Only $m>0$ harmonics are shown here. The differences of the $m\le 0$ harmonics between the vacuum RMP and response RMP are minor (which can be roughly recognized from Fig. 8) and are thus not shown here.

timescale of slowing-down time (∼100 ms for typical parameters of EAST tokamaks). A steady state is reached when there is a balance between the source (beam injection and ionization) and sink (thermalization and edge loss). In this section, we examine the steady state of the radial profiles of NBI heating power density and fast ion pressure.

Figure 10(a) compares the radial profiles of the NBI heating power density delivered to bulk ions between the case without RMP and those with RMPs of $\Delta\Phi=0,\pi$. To clearly show the difference, Fig. 10(b) plots the power density difference ΔH_i, where $\Delta H_i \equiv H_i^{(\mathrm{rmp})} - H_i^{(\mathrm{normp})}$ is the power density difference between the case with RMP and that without RMP. The results indicate that the ion heating power density is significantly reduced near the edge (around the radial location $q=3$) by the RMPs of $\Delta\Phi=0$ while very marginal reduction is induced by the RMP of $\Delta\Phi=\pi$. The results also show that the heating power density is slightly increased around $q=2$ by the RMPs.

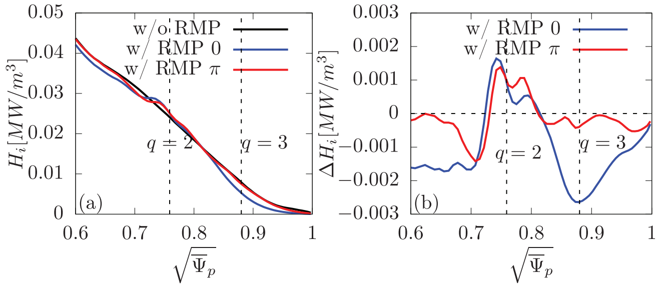

FIG. 10. (a) Radial profiles of NBI heating power density delivered to bulk ions. (b) Difference of ion heating power density between the case with RMP and that without RMP. The locations of $q=2$ and $q=3$ rational surfaces are indicated. The FLR effect is included in the simulations.

The radial profile of NBI heating power density is determined by the radial profile of fast ion pressure (see Appendix D for the formula of computing the power density). Figure 11(a) plots the radial profile of fast ion pressure for the three cases: without RMP, with RMP of $\Delta\Phi=0$, and with RMP of $\Delta\Phi=\pi$. To clearly show the difference, Fig. 11(b) plots the pressure difference ΔP_f, where $\Delta P_f \equiv P_f^{(\mathrm{rmp})} - P_f^{(\mathrm{normp})}$ is the power density difference between the case with RMP and that without RMP. The results indicate that the influence of RMPs on fast ion pressure is similar to that of RMPs on the ion heating power, i.e., the pressure is significantly reduced near the edge (around the radial location $q=3$) by the RMPs of $\Delta\Phi=0$ while very marginal reduction is induced by the RMP of $\Delta\Phi=\pi$ and the pressure is slightly increased around $q=2$ by the RMPs.

As is shown in Fig. 11, the pressure increasing around $q=2$ surface induced by RMPs is quite small. It is reasonable to doubt whether the increasing is physical or due to numerical errors. As a partial verification of this issue, we perform convergence studies over some numerical parameters used in the simulations such as the maker numbers and time step sizes. Figure 12 shows that the radial profiles of ΔP_f agree with each other for two different values of the time step size and marker number. Also shown in Fig. 12 is the dependence of values of ΔP_f at a specified radial location ($\rho=0.755$) over the time step size and marker number, which shows reasonable convergence.

It is not surprising to observe the local increasing of fast ion pressure when a RMP is imposed. RMPs generally have pump-out effects on fast ions. However, the pump-out effects can be non-uniform along the radial direction, which implies that some radial locations may accumulate fast ions, resulting higher fast ion pressure than the no RMP case.

The results in Fig. 11(b) indicate that the radial fluctuation of fast ion pressure relative to the no RMP case depends on the RMP up-down phase difference $\Delta\Phi$: radial fluctuation for $\Delta\Phi=0$ is larger than the case of $\Delta\Phi=\pi$. To understand this, we compare the resonant and non-resonant components for the two phasings. The amplitude of resonant components is related to the width of magnetic

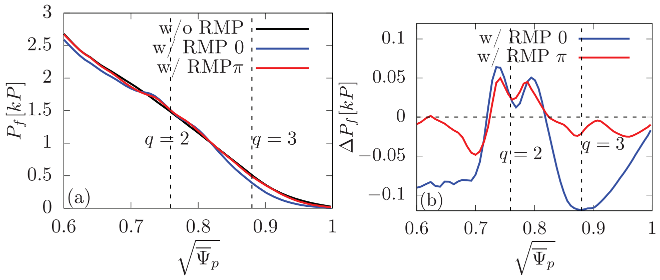

FIG. 11. (a) Radial profiles of fast ion pressure. (b) Difference of fast ion pressure between the case with RMP and that without RMP.

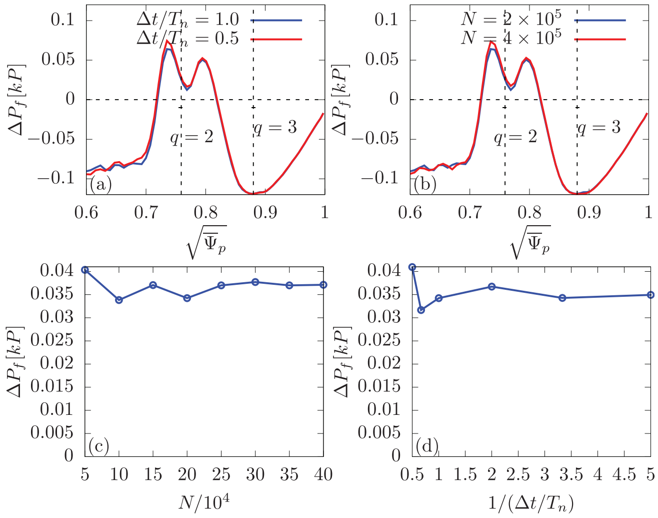

FIG. 12. Comparison of radial profiles of fast ion pressure perturbation for different values of time step sizes (a) and marker number (b). Panel (c) plots the ΔP_f at $\sqrt{\Psi_p} = 0.755$ as a function of number of markers used in the simulation. Panel (c) plots the ΔP_f as a function of the inverse of the time step size $1/(\Delta t/T_n)$, where $T_n = 2\pi/(B_n Z_f e/m_f)$ with $B_n = 1T$. RMP of $\Delta\Phi = 0$ is used in the simulations. In (a) and (d), marker number $N = 2\times10^5$. In (b) and (c), time step size $\Delta t/T_n = 1.0$.

islands [Eq. (4)], which can be inferred from Poincare sections of magnetic field lines. Figure 13 shows the Poincare plots of magnetic field line for RMPs of $\Delta\Phi = 0$ and $\Delta\Phi = \pi$. The results indicate that magnetic islands for RMP of $\Delta\Phi = 0$ are wider than those of $\Delta\Phi = \pi$. The magnetic island width can also be directly calculated by using Eq. (4). The results are plotted in Fig. 14(a), which confirm the conclusion draw from the Poincare plots.

The values of Chirikov parameter σ at the rational surfaces $q = 2, 3, 4, 5$ are plotted in Fig. 14(b), which indicates $\sigma > 1$ at $q = 5$ for $\Delta\Phi = 0$ RMP while σ is still less than one at $q = 5$ for $\Delta\Phi = \pi$ RMP. This implies that the radial width of stochastic magnetic field is larger for $\Delta\Phi = 0$ RMP than that of $\Delta\Phi = \pi$ RMP.

The width of magnetic islands characterizes the amplitude of resonant components. To characterize the non-resonant components, Fig. 15 plots the radial profiles of amplitude of various poloidal Fourier harmonics. The radial peaks of the harmonics can be used as a measure of magnitude of non-resonant harmonics. The results clearly show that amplitude of the non-resonant components (except for $m = 1$) for $\Delta\Phi = 0$ are larger than those of $\Delta\Phi = \pi$.

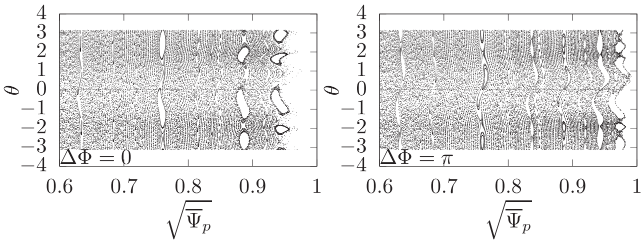

FIG. 13. Comparison of magnetic field line Poincare plots between RMP of $\Delta\Phi = 0$ and that of $\Delta\Phi = \pi$.

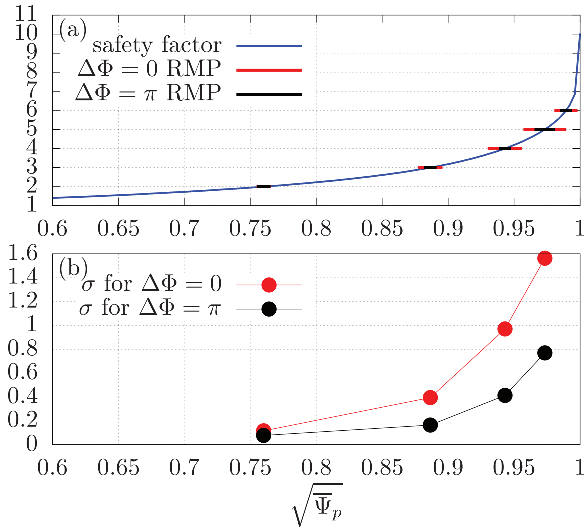

FIG. 14. Magnetic island width (upper panel) and Chirikov parameter values (low panel) for RMPs of $\Delta\Phi = 0$ and $\Delta\Phi = \pi$. The safety factor profile is also shown to indicate the radial locations of rational surfaces. The island width is calculated by using formula (4).

The above results indicate that both resonant components and non-resonant components of RMP of $\Delta\Phi = 0$ are larger than those of $\Delta\Phi = \pi$. Both the resonant components and non-resonant components can contribute to the redistribution of fast ions. Therefore, the

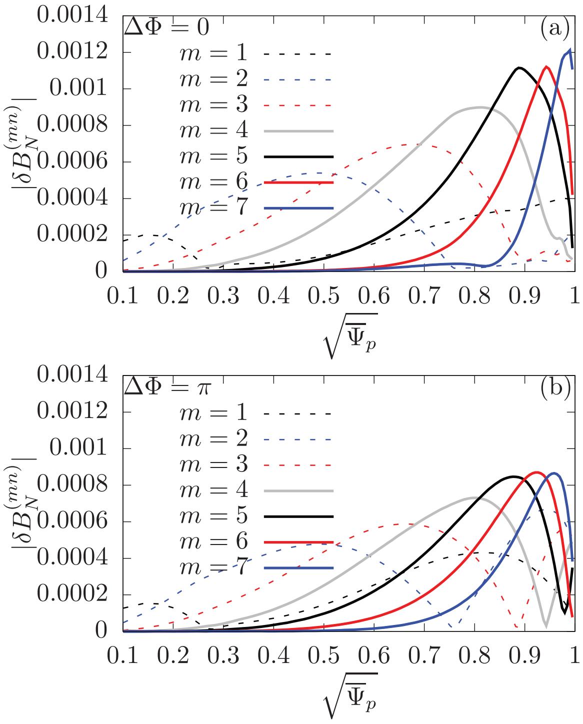

FIG. 15. Radial profiles of poloidal Fourier harmonics of $n = 1$ RMPs of $\Delta\Phi = 0$ (a) and $\Delta\Phi = \pi$ (b).

larger fluctuation of fast ion pressure for the case of $\Delta\Phi = 0$ is probably due to the larger resonant and non-resonant components for this coil current configuration.

Plasma response usually helps heal magnetic islands, i.e., reduces the resonant components, as is shown in Figs. 8 and 9, and thus is believed to be beneficial to fast ion confinement.[15] Figure 16 compares the steady-state fast ion profiles (subtracted by the profile when no RMP is imposed) between the vacuum RMP and response RMP. The results shows that the fast ion pressure around $q = 2$ for the response RMP is higher than that for the vacuum RMP, which suggests that plasma response is beneficial to fast ion confinement around the $q = 2$ surface. However, the results also show that the fast ion pressure within $\sqrt{\bar{\Psi}_p} \approx 0.65$ for the response RMP case is lower than the vacuum RMP case. This may be due to the enhancement of $m = 1$ and $m = 2$ harmonics at their non-resonant locations by the plasma response, as is shown by Fig. 9.

Since fast ion source from NBI is localized in a narrow toroidal span, it is natural to ask whether the toroidal phasing of RMPs relative to the fast ion source can have effects on the steady-state radial profile of fast ions. To answer this question, we compute the steady-state radial profile of fast ion pressure under various toroidal phasings while fixing the up-down phase difference $\Delta\Phi$. The results are plotted in Fig. 17 for $\Delta\Phi = \pi/2$, which indicate that the toroidal phasing has slight effects on the steady-state radial profile. One interesting observation is that the profiles around $q = 2$ are almost identical among the cases of different toroidal phasings.

The effect of toroidal phasing on radial profile being slight may be valid only for passing fast ions resulted from the tangential injection considered in this paper. In Ref. 34, the toroidal phasing is found to have significant effects on the fast ion confinement, where both passing and trapped particles are significant in the fast ion source.

V. UP-DOWN PHASE DEPENDENCE OF VOLUME INTEGRATED QUANTITIES

This section investigates the dependence of spatially integrated heating power, fast ion stored energy, and loss fraction on the RMP up-down phase difference $\Delta\Phi$. The results are shown in Fig. 18.

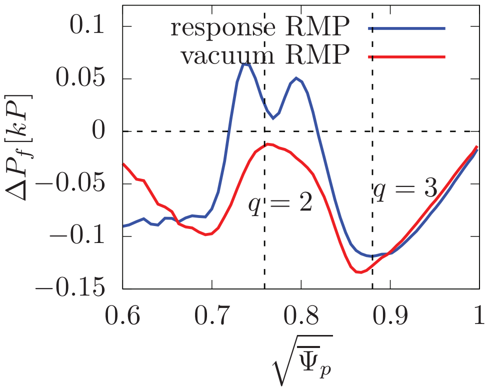

FIG. 16. Difference of steady-state fast ion pressure between the case with RMP and that without RMP. The blue curve is for the RMP with plasma response while the red curve is for the vacuum RMP. Both the RMPs are of up-down phasing $\Delta\Phi = 0$.

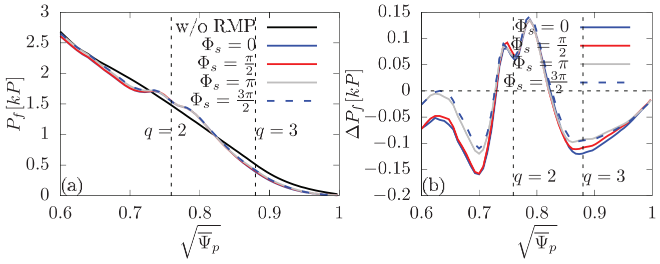

FIG. 17. (a) Radial profiles of fast ion pressure under RMPs of various toroidal phasings relative to the fast ion source, Φ_s. Also shown in (a) is the radial profile when RMPs are absent. (b) The difference between the case with RMP and that without RMP for various values of Φ_s. The up-down phase difference $\Delta\Phi$ is fixed at $\pi/2$. The results indicate that the toroidal phasing has slight effect on the steady-state radial profile of fast ions.

The first observation from Fig. 18 is that the heating power and fast ion stored energy are reduced relative to the no RMP case and the loss fraction is increased relative to the no RMP case. Figure 18 shows that the results for full vacuum RMP and the filtered vacuum RMP (keeping only the $n = \pm 1$ Fourier harmonic) agree with each other well, indicating harmonics other than $n = \pm 1$ have negligible effects. The results also indicate that the heating powers and fast ion stored energy are roughly decreasing functions of the loss fraction in all the three cases, as is expected.

As is mentioned above, plasma response usually helps heal magnetic islands and thus is believed to be beneficial to fast ion confinement. Comparing between the response RMP case and the vacuum RMPs, however, we found the loss fraction in the response RMP case is not always smaller the corresponding vacuum case. This may indicate that non-resonant components, which can be enhanced when plasma response is included, have significant effects on fast ion confinement.

To more accurately describe the magnetic stochasticity, we use a purely numerical method to determine the radial width of stochasticity (rather than using the approximate analytical formula of magnetic island width and the Chirikov magnetic island overlap criteria discussed above). Figure 19 plots the radial width of stochastic magnetic field as a function of the RMP coil up-down phase difference $\Delta\Phi$. The radial width is determined numerically by tracing a series of field lines starting from the low field side midplane (i.e., $\theta = 0$, $\phi = [0:2\pi]$, and $\rho_p = [0:1]$). If a field line touches the wall during its first 3000 toroidal transits, then the magnetic field is considered as stochastic at the initial radial location. At each toroidal location, scanning the initial points from the core to the edge, the radial innermost location where magnetic field becomes stochastic determines the width of the stochastic region. This will give different value of radial width at different toroidal locations. The reasonable radial width of stochasticity should be the toroidal maximal values. This width is denoted by w_{s1} in Fig. 19. As a comparison, the toroidal minimal values and toroidal average values of the width of stochasticity, denoted by w_{s2} and w_{s3}, respectively are also shown in Fig. 19. The results show that the dependence of fast ion loss fraction on $\Delta\Phi$ roughly agrees with those of the radial width of stochasticity on $\Delta\Phi$.

VI. RESONANCE BETWEEN RMPS AND LOST FAST IONS

Fast ion loss induced by RMP is often related to the resonance between fast ions and RMPs. Generally, the resonance condition in tokamaks between a wave and a particle drift is given by

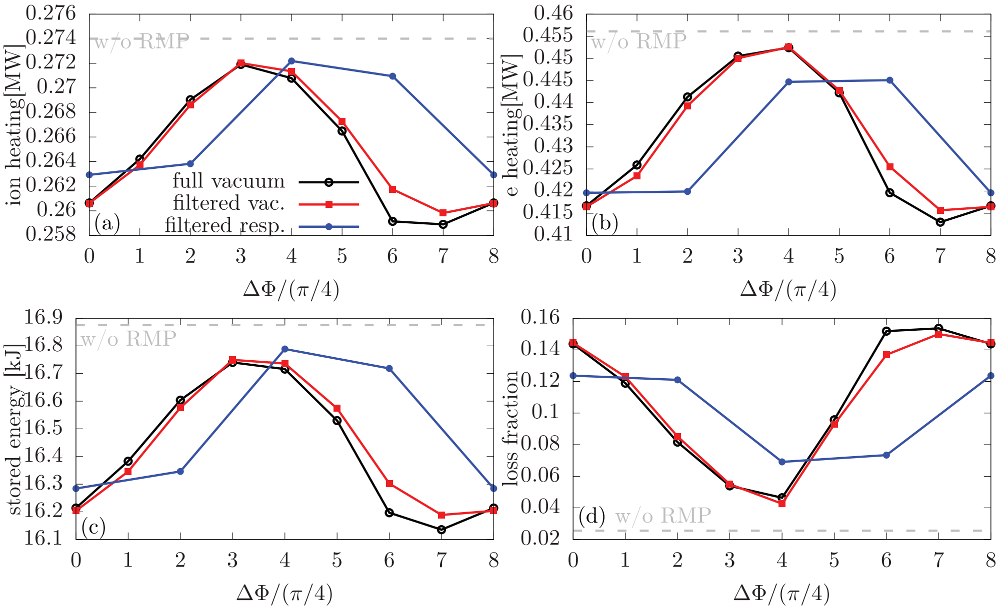

FIG. 18. The up-down phasing dependence of (a) ion heating power, (b) electron heating power, (c) fast ion stored energy, and (d) fast ion loss fraction. The corresponding values in the no RMP case are shown for comparison. The results for three kinds of magnetic perturbations are shown, namely, full vacuum magnetic perturbation generated by the coils (without filtering), filtered vacuum field (keeping only the $n = \pm 1$ Fourier harmonic), and the filter response RMP.

$$n\omega_\phi - \omega = p\omega_\theta, \qquad (6)$$

where n and ω are the toroidal mode number and angular frequency of the wave, respectively, ω_ϕ and ω_θ are the toroidal angular frequency and poloidal angular frequency of the particle drift, respectively, and p can be called resonance order, which is an arbitrary rational number. When p is an integer, it is the usual resonance condition. When $p = j/k$ is a non-integer fraction (j and k are integers), the resonance is called fractional resonance,[35–38] where the (unperturbed) drift motion reach the same phase of the wave when it finish k times of poloidal periods. The fractional resonance is often considered to be important when the wave amplitude is large and thus might be related to the nonlinear effects. However, the definition of resonance given above is essentially linear because we are using the unperturbed motion in defining ω_ϕ and ω_θ.

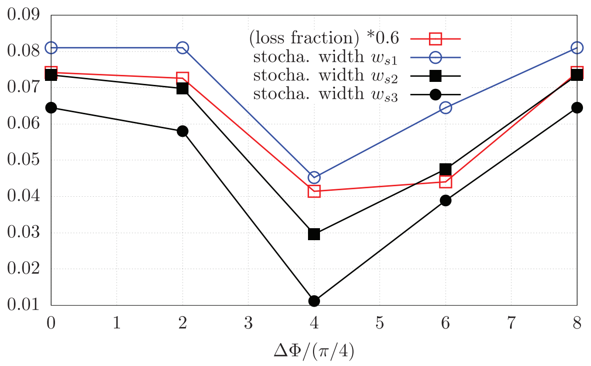

FIG. 19. Radial width of stochastic magnetic field as a function of the RMP coil up-down phase difference ΔΦ. The width is defined in terms of the square root of the normalized poloidal magnetic flux, $\rho = \sqrt{\bar{\Psi}_p}$ and is defined as the difference of ρ between the stochastic radial location and the unperturbed last closed-flux surface. Three possible radial width, namely, w_{s1}, w_{s2}, w_{s3}, are plotted. Also plotted is the dependence of the loss fraction on the phase difference ΔΦ.

For RMPs with $\omega = 0$ and $n = 1$ considered in this work, the resonance condition in Eq. (6) is simplified as

$$p = \frac{\omega_\phi}{\omega_\theta}. \qquad (7)$$

To show how important the resonant effects are in generating fast ion loss, we propose to use the graph of $\omega_\phi/\omega_\theta$ vs Δf, where $\Delta f = f_{\rm rmp} - f_{\rm normp}$ is the difference of the lost fast ion distribution function between the case with RMP and that without RMP. By taking the difference, we exclude all the fast ions that are lost due to the first-orbit prompt loss and pure collision loss.

For the tangential NBI considered in this work, the results indicate that lost particles are dominated by passing particles and we will consider only passing particles here. The graph of $\omega_\phi/\omega_\theta$ vs Δf for lost passing ions is plotted in Fig. 20 for RMPs of $\Delta\Phi = 0, \pi/2, \pi, 3\pi/2$. The values of $\omega_\phi/\omega_\theta$ at peaks of Δf are indicated in Fig. 20, which shows that some of them cannot be well approximated by integers.

As is indicated in Fig. 20, some peaks of Δf seem to appear at non-integer fractions. It is usually believed that fractional resonances are associated with the nonlinear effects and thus amplitude of the perturbation matter. In the work of Kramer *et al.*,[37] the fractional resonance appears when the amplitude of the wave exceeds a threshold and thus it is natural to connect the fraction resonance with nonlinear effects. Here, we examine how peaks of Δf change with the changing

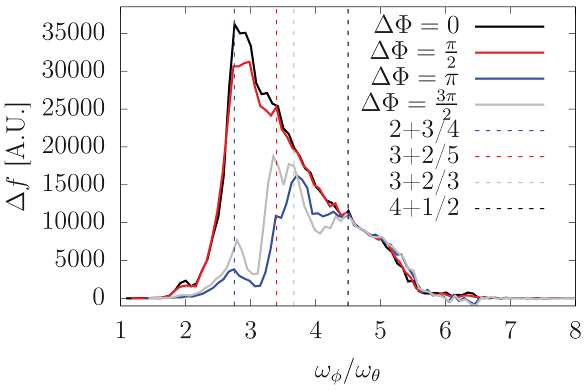

FIG. 20. The difference of distribution of lost passing particles relative to the no RMP case for various RMP up-down phasings $\Delta\Phi$. The results show that some peaks of Δf appear at non-integer values of p. The small peak at $p = 2$ is probably due to resonance of integer order. The peaks at $p = 2 + 3/4$ can be roughly regarded to be due to resonance of integer order, considering that the peaks are of finite width and are close to $p = 3$. The peaks at $p = 3 + 2/5$, $p = 2 + 2/3$ and $p = 4 + 1/2$ cannot be well approximated as near integer values of p.

of amplitude of coil currents. The results are plotted in Fig. 21, where the peaks remain at the same non-integer values when the current amplitude is changed from 10 kA (the designed maximal total current in RMP coils on EAST) to 2 kA. The fact that these peaks persist even when the RMP amplitude is very small (2 kA) may imply that the peaks at these non-integer values of $\omega_\phi/\omega_\theta$ are not related to nonlinear effects.

We note that linear resonances can be of non-integer fractional orders (it is easy to demonstrate this by deriving the resonance condition from scratch[38]) Since, as mentioned above, it is hard to relate the peaks at non-integer fraction with nonlinear effects, a plausible interpretation for these peaks is that they are due to linear resonances of non-integer fractional orders.

We note that resonance is not a necessary condition for RMP to induce fast ion loss (resonance is only a beneficial case for perturbation to have large impact). Any perturbation that breaks the axisymmetry can potentially generate radial particle transport and hence loss. Therefore, we cannot exclude the possibility that the peaks at non-integer values are caused by non-resonant effects of RMPs on fast ions. This is one of the limitations of this crude statistical method in identifying resonance.

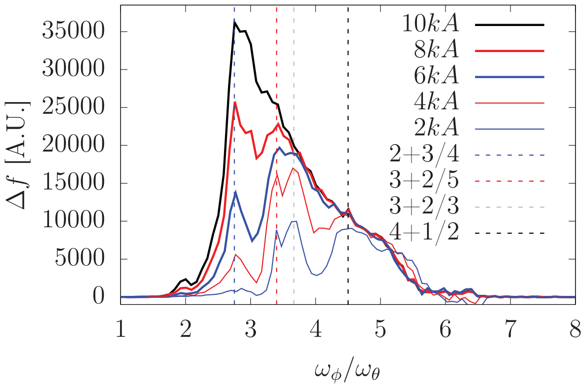

FIG. 21. The same as Fig. 20 except that the RMP up-down phasing is fixed at $\Delta\Phi = 0$, and the amplitude of the coil current is scanned.

Another observation from Fig. 21 is that the peaks are of nonzero expansion width, so that the consecutive peaks are not well separated, which makes it difficult to identify all peaks in some cases (e.g., for the case of 10 kA RMP, only the peaks near $p = 2$, 3 show up and all the other peaks merge and are blurred).

Since there are obvious statistic noises in the results of Figs. 20 and 21, we need to make sure that the dominant peaks identified above are not sensitive to the noise. We perform a numerical convergence study over the number of markers N used in the simulation (which is the most important numerical parameter in reducing noise). The results are plotted in Fig. 22, which shows that the statistic noise does no significantly change the peaks in Δf, i.e., the results are well converged, in terms of the dominant resonant peaks.

In the above, Δf is the difference of the lost fast ion distribution function between the case with RMP and that without RMP. Collisions are included in both the cases. By taking the difference, we expect to cancel the collision effect and obtain the pure RMP effect. However, collision may blur the resonance between RMPs and fast ions if the collision effects are not exactly canceled out in the simple subtraction. Thus, it is desirable to do a simulation with collisions turned off. The results are plotted in Fig. 23 for RMPs of $\Delta\Phi = 0, \pi/2, \pi, 3\pi/2$, which show a similar behavior as that in Fig. 20. Specifically, there are peaks at non-integer values of p (e.g., peaks between $p = 3$ and $p = 4$ for the $\Delta\Phi = \pi$ and $\Delta\Phi = 3\pi/2$ RMPs). There are also some peaks which are very near to integer values of p (e.g., the peak near $p = 3$ for the $\Delta\Phi = \pi/2$ RMP).

VII. SUMMARY AND DISCUSSION

The effects of resonant magnetic perturbation on the steady-state radial profile of neutral beam heating and fast ion pressure are studied computationally in a realistic tokamak configuration. It is observed in the simulations that RMPs can accumulate fast ions at some radial locations, giving a higher fast ion pressure than the case without RMP. RMPs generally have pump-out effects on fast ions. The pump-out effects are non-uniform along the radial direction, which implies that some radial locations may accumulate fast ions. Therefore, it is not surprising to observe the local increasing of fast ion pressure when a RMP is imposed.

It is also found that the toroidal phasing of the RMP with respect to the fast ion source has slight effects on the steady-state radial profile

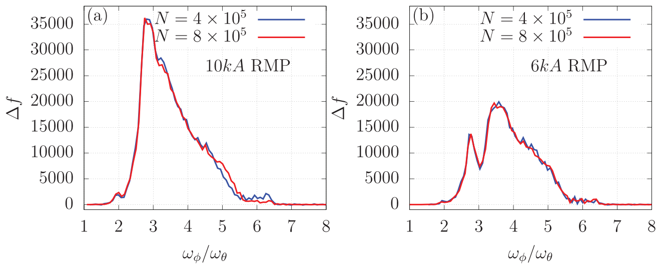

FIG. 22. Convergence of Δf over number of markers N for RMPs of currents 10 kAt (left) and 6 kAt (right). RMPs of $\Delta\Phi = 0$ are used in the simulation.

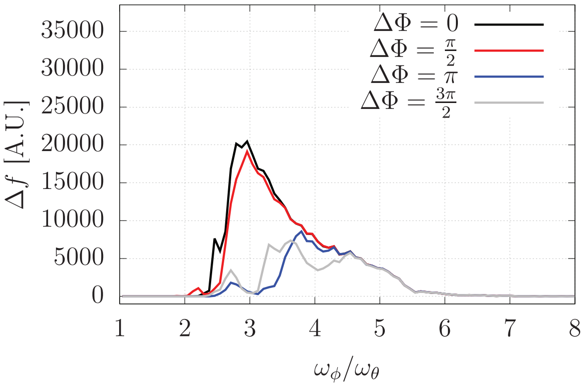

FIG. 23. The same as Fig. 20 except that collisions are turned off in this case. The peaks of Δf roughly agree with those in Fig. 20. The results also show that the amplitude of Δf in the collisionless case is much smaller than that in the collisional case (Fig. 20). The unit of Δf is the same as that of Fig. 20.

of fast ions. The effect being slight is expected, considering that most particles resulted from the tangential injection are passing particles which quickly traverse a full toroidal loop, making the relative location between neutral beam source and RMP coils almost irrelevant. For trapped particles resulted from perpendicular NBI whose toroidal procession frequencies are low, the toroidal phase of RMP coils relative to the source can be important since the trapped particles can remain in a limited toroidal range for a sufficient time. The toroidal phasing can be a useful free parameter for fast ion control using RMPs, considering that ELMs control is not sensitive to the toroidal phasing.

The dependence of fast ion loss fraction on the RMP up-down phase difference is found to show a similar behavior as the dependence of the radial width of chaotic edge magnetic field on the up-down phase difference.

A simple numerical statistical method, which uses the lost fast ion distribution over $\omega_\phi/\omega_\theta$, is proposed to identify the resonance between lost fast ions and RMPs. Using this method, we found that the RMP-induced loss of passing particles may be partially due to resonance of fractional orders. However, the reliability and usefulness of this statistic method in identifying resonance between lost fast ions and RMPs need to be further explored. Most authors analyze the fast ion transport in terms of the variation of the toroidal canonical momentum, δP_ϕ, which is a more informative figure of merit than the simple condition of loss or not (used in this work), in revealing the resonance between fast ions and magnetic perturbations.[18]

ACKNOWLEDGMENTS

One of the authors (Y.H.) acknowledges useful discussions with Dr. Nong Xiang and Dr. Wei Chen. Numerical computations were performed on Tianhe at National Super-Computer Center in Tianjin and the ShenMa computing cluster in Institute of Plasma Physics, Chinese Academy of Sciences. This work was supported by National Key R&D Program of China under Grant No. 2017YFE0300400, by Comprehensive Research Facility for Fusion Technology Program of China under Contract No. 2018-000052-73-01-001228, by users with Excellence Program of Hefei Science Center CAS under Grant No. 2021HSC-UE017, and by the National Natural Science Foundation of China under Grant No. 11575251.

AUTHOR DECLARATIONS

Conflict of Interest

The authors have no conflicts to disclose.

DATA AVAILABILITY

The data that support the findings of this study are available from the corresponding author upon reasonable request.

APPENDIX A: NEUTRAL PARTICLE SOURCE

Neutral particle source is implemented by using the Monte Carlo method and taking into account the beam focus and divergence, the shape of the accelerating grids, and the spatial distribution of particles on the exit grid. Figure 24 shows a sketch map of the accelerating grids of EAST neutral beam system.

The neutralizing process is not directly modeled in the simulation, and its effect is included only through the input number ratio between particles of the full (kinetic) energy, half energy, and 1/3 energy (the number ratio between them is assumed to be 80 : 14 : 6 in this paper, with the full energy being 51 keV). We assume that other beam properties (e.g., focus and divergence) are not changed by the neutralizing process, except that only part of the ions succeed in becoming neutrals. The NBI power after neutralizing is assumed to be 1 MW. In this paper, we consider one of the four beams on EAST, which is injected in the co-current direction, with the tangent radius of the central beam being 1.26 m.

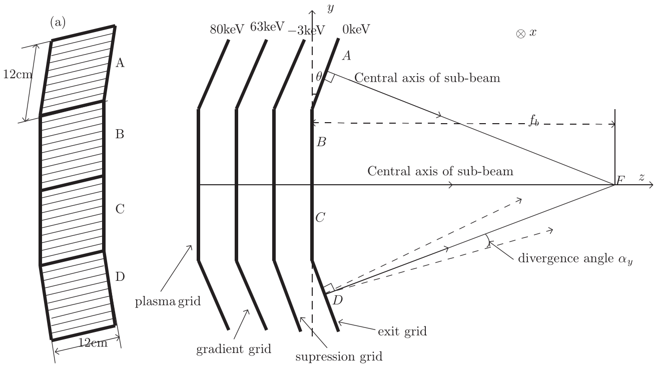

FIG. 24. Left: Three-dimensional sketch map of one of the accelerating grids. Right: Side view of the four groups of accelerating grids of EAST neutral beam injector, which are, respectively, called plasma grid, gradient grid, suppression grid, and exit grid. A typical setting of voltage on the grids is indicated on the graph. Each accelerating grid has four sub-grids, indicated by A, B, C, and D on the figure. Each sub-grid is a 12 cm × 12 cm square. Sub-grids A and D are rotated with respect to the central sub-grids B and C by a small angle $\theta = (1\frac{1}{12})^\circ$. This angle is exaggerated on the figure. The central axis of the two beams from grids A and D intersect at F. The vertical focal length f_b is defined as the distance from point F to the plane of BC grids ($f_b \approx 9.5\,\mathrm{m}$). The horizontal focal length is infinite. The $y = 0$ plane corresponds to the tokamak midplane. The beam horizontal and vertical divergence angles are set to be 0.6° and 1.2°, respectively.

APPENDIX B: IONIZATION IN TOKAMAK PLASMA

The neutral particle trajectories are assumed to be along straight lines until they arrive at the ionization locations in the plasma. The Monte Carlo method of implementing the ionization process is as follows.[6] First define ν by

$$\nu = n_i\sigma_{\mathrm{ch}} + n_i\sigma_i + n_e\frac{\langle\sigma_e v_e\rangle}{v_b}, \tag{B1}$$

where n_i and n_e are the number density of background plasma ions and electrons, respectively, σ_{ch} is the cross section for charge exchange with plasma ions, σ_i is the cross section for ionization by plasma ions, $\langle\sigma_e v_e\rangle$ is the electron impact ionization rate coefficient averaged over the Maxwellian distribution, $\langle\sigma_e v_e\rangle/v_b$ is the effective cross section of the electron impact ionization, where v_b is the neutral particle velocity. Then, associate each marker loaded with a random number η that is uniformly distributed in $[0, 1]$. Then, along the trajectory of each neutral particle (straight line), the integration $s = \int_0^l \nu(l')dl'$ is calculated to examine whether $s \geq \ln(1/\eta)$ or not. If $s \geq \ln(1/\eta)$, the neutral particle is considered to be ionized. The value of ν outside the last closed flux surface (LCFS) is set to be zero, i.e., the ionization outside LCFS is not considered. The ionization cross-section data used in this work are from the ADAS database (https://open.adas.ac.uk/) and Janev's paper.[39]

The Monte Carlo implementation gives the ionization locations of each marker loaded in the simulation. These locations are used as initial conditions in the subsequent orbit following computations. Those neutral particles that are not yet ionized when they reach the inner wall of the device are lost to the wall and this loss are called shine-through loss.

APPENDIX C: GUIDING-CENTER MOTION AND FINITE LARMOR RADIUS EFFECT

Knowing the birth location $\mathbf{x}$ of a fast ion (given by the module calculating the neutral particle ionization), the corresponding guiding-center location $\mathbf{X}$ is calculated via the following guiding-center transform,

$$\mathbf{X} = \mathbf{x} + \mathbf{v} \times \frac{\mathbf{b}(\mathbf{x})}{\Omega(\mathbf{x})}, \tag{C1}$$

where $\mathbf{v}$ is the fast ion velocity, $\mathbf{b} = \mathbf{B}/B$, $\Omega = BZ_f e/m_f$ is the cyclotron angular frequency, m_f and $Z_f e$ are the mass and charge of the fast ion, respectively, and $\mathbf{B}$ is the magnetic field.

The guiding-center drift of each fast ion is then followed by numerically integrating the following guiding center motion equation,[40]

$$\frac{d\mathbf{X}}{dt} = \frac{\mathbf{B}^\star}{B_\parallel^\star}v_\parallel + \frac{\mu}{m_f\Omega B_\parallel^\star}\mathbf{B}\times\nabla B \tag{C2}$$

$$\frac{dv_\parallel}{dt} = -\frac{\mu}{m_f}\frac{\mathbf{B}^\star}{B_\parallel^\star}\cdot\nabla B, \tag{C3}$$

where $v_\parallel$ is the parallel (to the magnetic field) velocity and μ is the magnetic moment (a constant of motion) defined by $\mu = m_f v_\perp^2/(2B)$ with $v_\perp$ being the perpendicular speed; $\mathbf{B}^\star$ and $B_\parallel^\star$ are defined by

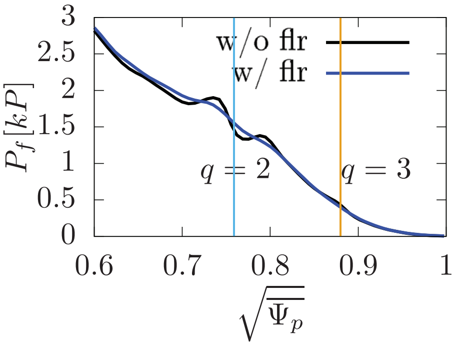

FIG. 25. Comparison of radial profiles of fast ion pressure between the case when the FLR effect is taken into account and that when it is neglected. The FLR effect is taken into account when checking whether particles touch the first wall in both the cases. RMP of $\Delta\Phi = 0$ is used.

$$\mathbf{B}^\star = \mathbf{B} + B\frac{v_\parallel}{\Omega}\nabla\times\mathbf{b} \tag{C4}$$

$$B_\parallel^\star \equiv \mathbf{b}\cdot\mathbf{B}^\star = B\left(1 + \frac{v_\parallel}{\Omega}\mathbf{b}\cdot\nabla\times\mathbf{b}\right), \tag{C5}$$

respectively.

The cylindrical coordinates (R, ϕ, z) are adopted in writing the component equations of guiding-center motion. Using the cylindrical coordinates (rather than magnetic coordinates) has the advantage that we can handle orbits on the magnetic axis and outside the LCFS without difficulties. The fourth-order Runge–Kutta scheme is used in integrating the equations. Orbits outside the LCFS are followed until they touch the wall.

The FLR effect is taken into account by evaluating and averaging the magnetic fields in Eqs. (C2) and (C3) on a gyro-ring (four points average is used in the simulation). The gyro-ring is approximated by a circle in the poloidal plane with the Larmor radius calculated by using the toroidal magnetic field at the guiding-center location. When checking whether a fast ion touches the wall, four points on the gyro-ring are also calculated. If any one of the four points touches the wall, the fast ion is considered as lost.

The FLR effect is also taken into account when depositing markers to compute fast ion pressure. Neglecting the FLR effect in this case will give significantly different radial profile of fast ion steady-state pressure, as is show in Fig. 25, which indicates that there is a significant averaging effect from the large Larmor radius of fast ions.

APPENDIX D: FAST ION COLLISIONS AND HEATING POWER DENSITY

The collision model of fast ions with the background electrons and ions adopted in TGCO includes the effects of the slowing-down, energy diffusion, and pitch angle scattering.

The birth velocity of the fast ions from NBI is much larger than the thermal velocity of background ions but still much smaller than the electron thermal velocity, i.e.,

$$v_{ti} \ll v_f \ll v_{te}. \tag{D1}$$

(This condition is still valid for the fast alpha particles in reactor plasmas.) Using this condition, the collision term of fast ions with the background Maxwellian electrons and ions can be simplified. Specifically, the Monte Carlo implementation of the resulting collision operator takes the form given in Refs. 41 and 42. For reference ease, we repeat it here. In the Monte Carlo implementation, the pitch-angle variable $\lambda = v_\parallel / v$ and velocity v are altered at the end of each time step according to the following scheme:

$$\lambda_{\rm new} = \lambda_{\rm old}(1-\nu_d\Delta t) \pm \sqrt{(1-\lambda_{\rm old}^2)\nu_d\Delta t} \tag{D2}$$

and

$$\begin{aligned} v_{\rm new} = v_{\rm old} - v_{\rm old}\nu_s\Delta t\left[1+\left(\frac{v_c}{v_{\rm old}}\right)^3\right] \\ +\frac{\nu_s\Delta t}{m_f v_{\rm old}}\left[T_e - \frac{1}{2}T_i\left(\frac{v_c}{v_{\rm old}}\right)^3\right] \\ \pm\sqrt{\frac{\nu_s\Delta t}{m_f}\left[T_e + T_i\left(\frac{v_c}{v_{\rm old}}\right)^3\right]}, \end{aligned} \tag{D3}$$

where ± is randomly chosen with equal probability for plus and minus, Δt is the time step, and ν_d is the velocity-dependent pitch-angle scattering rate given by

$$\nu_d = \frac{Z_{\rm eff}}{v^3}\Gamma^{f/e}., \tag{D4}$$

with $\Gamma^{f/e}$ defined by

$$\Gamma^{f/e} = \frac{n_e Z_f^2 e^4}{4\pi\epsilon_0^2 m_f^2}\ln\Lambda^{f/e}, \tag{D5}$$

where $Z_{\rm eff}$ is the effective charge number of background ions ($Z_{\rm eff} = 1$ in this work since we assume a pure Deuterium plasma without impurities) and Z_f is the fast ion charge number ($Z_f = 1$ in this work). ϵ_0 and $\ln\Lambda^{f/e}$ are, respectively, vacuum dielectric constant and the Coulomb logarithm. In Eq. (D3), ν_s is the fast ion slowing down rate due to the background electrons and is given by

$$\nu_s = \frac{4}{3\sqrt{\pi}}\frac{m_f}{m_e}\frac{\Gamma^{f/e}}{\left(\sqrt{2T_e/m_e}\right)^3}. \tag{D6}$$

In Eq. (D3), v_c is the critical velocity (at which the friction due to background ions is equal to that due to background electrons) given by

$$v_c = \left(\frac{3\sqrt{\pi}}{4}\frac{m_e}{m_i}\right)^{1/3}\sqrt{\frac{2T_e}{m_e}}. \tag{D7}$$

The scheme in Eq. (D2) models the pitch-angle scattering (due to background ions only). The first line of Eq. (D3) models the slowing-down (due to both background electrons (the "1" term) and ions [the $(v_c/v_{\rm old})^3$ term)] and the second line models the energy diffusion (due to both background ions and electrons). Collisions between fast ions themselves are ignored.

As a simple verification of the implementation of the numerical slowing-down model, Fig. 26 compares the numerical steady state velocity distribution function and the analytic slowing-down distribution function, which shows good agreement between them. The analytic slowing-down distribution is given by

$$f_v \propto \frac{v^2}{\left(1+(v/v_c)^3\right)}, \tag{D8}$$

where v_c is the critical velocity given by Eq. (D7). The numerical result was obtained in a simplified setting by turning off orbiting (hence no edge loss) and assuming uniform plasma profile, no energy diffusion, and injection with single energy of 51 keV in EAST discharge #52340@3.4s.

The heating power (due to fast ions) to bulk plasma within a given spatial volume V is equal to the fast ion kinetic energy loss rate within that volume, i.e.,

$$P = \sum_{j=1}^{N} w_j\frac{\Delta E_j}{\Delta t}, \tag{D9}$$

where N is the number of markers within the given spatial volume, w_j is the marker weight, ΔE_j is the kinetic energy decrease in a marker during the time interval Δt. Using $\Delta E_j = \frac{1}{2}m_f v_{j,\rm old}^2 - \frac{1}{2}m_f v_{j,\rm new}^2$, and the slowing-down algorithm, expression (D9) is written as

$$P = \frac{1}{2}m_f\sum_{j=1}^{N} w_j\left[2v_{j,\rm old}^2\nu_s(C_i+C_e) - v_{j,\rm old}^2\nu_s(C_i+C_e)^2\nu_s\Delta t\right],$$

where $C_i = (v_c/v_{j,\rm old})^3, C_e = 1$. Neglecting the second term, which is smaller than the first term by a factor of $\nu_s\Delta t \ll 1$, the above expression is written as

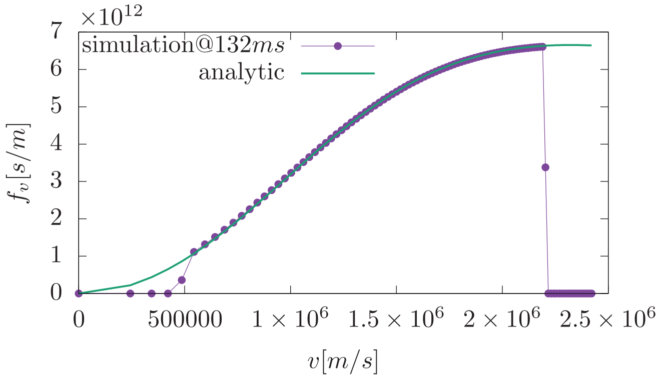

FIG. 26. Comparison between the numerical steady state velocity distribution function and the analytic slowing-down distribution function. The distribution function is defined by $f_v dv = dN$ with dN being the number of particles with velocity in $[v, v+dv]$. There is a discrepancy in the small velocity region because we consider particles of kinetic energy less than $2T_{i0}$ as thermalized and do not include their contribution to the fast ion distribution. There is a numerical jump at the injection energy since no particles are accelerated to higher energy (energy diffusion could make this jump smoother if included).

$$\begin{aligned} P &\approx \frac{1}{2} m_f \sum_{j=1}^{N} w_j \left[2 v_{j,\mathrm{old}}^2 \nu_s (C_i + C_e) \right], \\ &= P_i + P_e, \end{aligned} \tag{D10}$$

where

$$P_i = m_f \sum_{j=1}^{N} w_j v_{j,\mathrm{old}}^2 \nu_s C_i \tag{D11}$$

and

$$P_e = m_f \sum_{j=1}^{N} w_j v_{j,\mathrm{old}}^2 \nu_s C_e, \tag{D12}$$

which are the heating power delivered to the thermal ions and electrons, respectively.

The heating power densities are then given by $H_i = P_i/V$ and $H_e = P_e/V$.

REFERENCES

[1] J. Scoville, M. Boyer, B. Crowley, N. Eidietis, C. Pawley, and J. Rauch, Fusion Eng. Des. **146**, 6 (2019).

[2] C. Hu, Y. Xie, Y. Xie, S. Liu, Y. Xu, L. Liang, C. Jiang, P. Sheng, Y. Gu, J. Li, and Z. Liu, Plasma Sci. Technol. **17**, 817 (2015).

[3] M. Schneider, L.-G. Eriksson, I. Jenkins, J. Artaud, V. Basiuk, F. Imbeaux, T. Oikawa, and JET-EFDA Contributors and ITM-TF Contributors, Nucl. Fusion **51**, 063019 (2011).

[4] O. Asunta, J. Govenius, R. Budny, M. Gorelenkova, G. Tardini, T. Kurki-Suonio, A. Salmi, and S. Sipilä, Comput. Phys. Commun. **188**, 33 (2015).

[5] W. W. Heidbrink, M. Murakami, J. M. Park, C. C. Petty, M. A. V. Zeeland, J. H. Yu, and G. R. McKee, Plasma Phys. Controlled Fusion **51**, 125001 (2009).

[6] A. Pankin, D. McCune, R. Andre, G. Bateman, and A. Kritz, Comput. Phys. Commun. **159**, 157 (2004).

[7] B. Wan, Y. Liang, X. Gong, J. Li, N. Xiang, G. Xu, Y. Sun, L. Wang, J. Qian, H. Liu, X. Zhang, L. Hu, J. Hu, F. Liu, C. Hu, Y. Zhao, L. Zeng, M. Wang, H. Xu, G. Luo, A. Garofalo, A. Ekedahl, L. Zhang, X. Zhang, J. Huang, B. Ding, Q. Zang, M. Li, F. Ding, S. Ding, B. Lyu, Y. Yu, T. Zhang, Y. Zhang, G. Li, T. Xia, and EAST team and Collaborators, Nucl. Fusion **57**, 102019 (2017).

[8] B. Wan, Y. Liang, X. Gong, N. Xiang, G. Xu, Y. Sun, L. Wang, J. Qian, H. Liu, L. Zeng, L. Zhang, X. Zhang, B. Ding, Q. Zang, B. Lyu, A. Garofalo, A. Ekedahl, M. Li, F. Ding, S. Ding, H. Du, D. Kong, Y. Yu, Y. Yang, Z. Luo, J. Huang, T. Zhang, Y. Zhang, G. Li, T. Xia, and EAST team and Collaborators, Nucl. Fusion **59**, 112003 (2019).

[9] Y. Sun, M. Jia, Q. Zang, L. Wang, Y. Liang, Y. Liu, X. Yang, W. Guo, S. Gu, Y. Li, B. Lyu, H. Zhao, Y. Liu, T. Zhang, G. Li, J. Qian, L. Xu, N. Chu, H. Wang, T. Shi, K. He, D. Chen, B. Shen, X. Gong, X. Ji, S. Wang, M. Qi, Q. Yuan, Z. Sheng, G. Gao, Y. Song, P. Fu, B. Wan, and EAST Contributors, Nucl. Fusion **57**, 036007 (2016).

[10] Y. Sun, Y. Liang, Y. Q. Liu, S. Gu, X. Yang, W. Guo, T. Shi, M. Jia, L. Wang, B. Lyu, C. Zhou, A. Liu, Q. Zang, H. Liu, N. Chu, H. H. Wang, T. Zhang, J. Qian, L. Xu, K. He, D. Chen, B. Shen, X. Gong, X. Ji, S. Wang, M. Qi, Y. Song, Q. Yuan, Z. Sheng, G. Gao, P. Fu, and B. Wan, Phys. Rev. Lett. **117**, 115001 (2016).

[11] Y. Xu, L. Li, Y. Hu, Y. Liu, W. Guo, L. Ye, and X. Xiao, Nucl. Fusion **60**, 086013 (2020).

[12] Y. Xu, W. Guo, Y. Hu, L. Ye, X. Xiao, and S. Wang, Comput. Phys. Commun. **244**, 40 (2019).

[13] K. He, B. Wan, Y. Sun, M. Jia, T. Shi, H. Wang, and X. Zhang, Nucl. Fusion **59**, 126026 (2019).

[14] K. He, Y. Sun, B. Wan, S. Gu, and M. Jia, Nucl. Fusion **60**, 126027 (2020).

[15] K. He, Y. Sun, B. Wan, S. Gu, M. Jia, and Y. Hu, Nucl. Fusion **61**, 016009 (2020).

[16] M. Garcia-Munoz, S. Äkäslompolo, P. de Marne, M. G. Dunne, R. Dux, T. E. Evans, N. M. Ferraro, S. Fietz, C. Fuchs, B. Geiger, A. Herrmann, M. Hoelzl, B. Kurzan, N. Lazanyi, R. M. McDermott, M. Nocente, D. C. Pace, M. Rodriguez-Ramos, K. Shinohara, E. Strumberger, W. Suttrop, M. A. V. Zeeland, E. Viezzer, M. Willensdorfer, and E. Wolfrum, Plasma Phys. Controlled Fusion **55**, 124014 (2013).

[17] M. Garcia-Munoz, S. Äkäslompolo, O. Asunta, J. Boom, X. Chen, I. Classen, R. Dux, T. Evans, S. Fietz, R. Fisher, C. Fuchs, B. Geiger, M. Hoelzl, V. Igochine, Y. Jeon, J. Kim, J. Kim, B. Kurzan, N. Lazanyi, T. Lunt, R. McDermott, M. Nocente, D. Pace, T. Rhodes, M. Rodriguez-Ramos, K. Shinohara, W. Suttrop, M. V. Zeeland, E. Viezzer, M. Willensdorfer, and E. Wolfrum, Nucl. Fusion **53**, 123008 (2013).

[18] L. Sanchis, M. Garcia-Munoz, A. Snicker, D. A. Ryan, D. Zarzoso, L. Chen, J. Galdon-Quiroga, M. Nocente, J. F. Rivero-Rodriguez, M. Rodriguez-Ramos, W. Suttrop, M. A. V. Zeeland, E. Viezzer, M. Willensdorfer, F. Zonca, and ASDEX Upgrade Team and EUROfusion MST1 Team, Plasma Phys. Controlled Fusion **61**, 014038 (2018).

[19] K. Kim, H. Jhang, J. Kim, and T. Rhee, Phys. Plasmas **25**, 122511 (2018).

[20] M. A. V. Zeeland, N. M. Ferraro, W. W. Heidbrink, G. J. Kramer, D. C. Pace, X. Chen, T. E. Evans, R. K. Fisher, M. García-Muñoz, J. M. Hanson, M. J. Lanctot, L. L. Lao, R. A. Moyer, R. Nazikian, and D. M. Orlov, Plasma Phys. Controlled Fusion **56**, 015009 (2013).

[21] M. V. Zeeland, N. Ferraro, B. Grierson, W. Heidbrink, G. Kramer, C. Lasnier, D. Pace, S. Allen, X. Chen, T. Evans, M. García-Muñoz, J. Hanson, M. Lanctot, L. Lao, W. Meyer, R. Moyer, R. Nazikian, D. Orlov, C. Paz-Soldan, and A. Wingen, Nucl. Fusion **55**, 073028 (2015).

[22] K. G. McClements, R. J. Akers, W. U. Boeglin, M. Cecconello, D. Keeling, O. M. Jones, A. Kirk, I. Klimek, R. V. Perez, K. Shinohara, and K. Tani, Plasma Phys. Controlled Fusion **57**, 075003 (2015).

[23] K. Tani, M. Azumi, H. Kishimoto, and S. Tamura, J. Phys. Soc. Jpn. **50**, 1726 (1981).

[24] E. Hirvijoki, O. Asunta, T. Koskela, T. Kurki-Suonio, J. Miettunen, S. Sipilä, A. Snicker, and S. Äkäslompolo, Comput. Phys. Commun. **185**, 1310 (2014).

[25] R. B. White, N. Gorelenkov, W. W. Heidbrink, and M. A. V. Zeeland, Plasma Phys. Controlled Fusion **52**, 045012 (2010).

[26] G. J. Kramer, R. V. Budny, A. Bortolon, E. D. Fredrickson, G. Y. Fu, W. W. Heidbrink, R. Nazikian, E. Valeo, and M. A. V. Zeeland, Plasma Phys. Controlled Fusion **55**, 025013 (2013).

[27] D. Pfefferlé, W. Cooper, J. Graves, and C. Misev, Comput. Phys. Commun. **185**, 3127 (2014).

[28] X. XU, Y. XU, X. ZHANG, Y. HU, L. YE, and X. XIAO, Plasma Sci. Technol. **22**, 085101 (2020).

[29] Y. Q. Liu, A. Bondeson, C. M. Fransson, B. Lennartson, and C. Breitholtz, Phys. Plasmas **7**, 3681 (2000).

[30] Y. Liu, A. Kirk, and E. Nardon, Phys. Plasmas **17**, 122502 (2010).

[31] C. Cheng and M. Chance, J. Comput. Phys. **71**, 124 (1987).

[32] A. H. Boozer, Phys. Rev. Lett. **86**, 5059 (2001).

[33] Y. Sun, Y. Liang, J. Qian, B. Shen, and B. Wan, Plasma Phys. Controlled Fusion **57**, 045003 (2015).

[34] L. Sanchis, M. Garcia-Munoz, E. Viezzer, A. Loarte, L. Li, Y. Liu, A. Snicker, L. Chen, F. Zonca, S. Pinches, and D. Zarzoso, Nucl. Fusion **61**, 046006 (2021).

[35] W. W. Heidbrink and R. B. White, Phys. Plasmas **27**, 030901 (2020).

[36] L. CHEN and F. ZONCA, Plasma Sci. Technol. **21**, 125101 (2019).

[37] G. J. Kramer, L. Chen, R. K. Fisher, W. W. Heidbrink, R. Nazikian, D. C. Pace, and M. A. Van Zeeland, Phys. Rev. Lett. **109**, 035003 (2012).

[38] Y. Todo, Rev. Mod. Plasma Phys. **3**, 33 (2018).

[39] R. K. Janev and J. J. Smith, At. Plasma—Mater. Interact. Data Fusion **4**, 1 (1993).

[40] Y. Todo, Phys. Plasmas **13**, 082503 (2006).

[41] A. H. Boozer and G. Kuo-Petravic, Phys. Fluids **24**, 851 (1981).

[42] Y. Todo, M. V. Zeeland, A. Bierwage, and W. Heidbrink, Nucl. Fusion **54**, 104012 (2014).